Applied Catalysis B: Environmental 121–122 (2012) 30–39

Contents lists available at SciVerse ScienceDirect

Applied Catalysis B: Environmental

journal homepage: www.elsevier.com/locate/apcatb

# A comparative study on the removal of cylindrospermopsin and microcystins from water with NF-$TiO_2$-P25 composite films with visible and UV–vis light photocatalytic activity

Miguel Pelaez[a], Polycarpos Falaras[b], Athanassios G. Kontos[b], Armah A. de la Cruz[c], Kevin O'shea[d], Patrick S.M. Dunlop[e], J. Anthony Byrne[e], Dionysios D. Dionysiou[a,*]

[a] Environmental Engineering and Science Program, University of Cincinnati, Cincinnati, OH 45221-0012, USA
[b] Institute of Physical Chemistry, NCSR Demokritos, 15310 Aghia Paraskevi, Attiki, Greece
[c] Office of Research and Development, U.S. Environmental Protection Agency, Cincinnati, OH 45268, USA
[d] Department of Chemistry and Biochemistry, Florida International University, University Park, Miami, FL 3319, USA
[e] Nanotechnology and Integrated BioEngineering Centre, School of Engineering, University of Ulster, Northern Ireland, BT37 0QB, United Kingdom

ARTICLE INFO

*Article history:*
Received 11 January 2012
Received in revised form 2 March 2012
Accepted 6 March 2012
Available online 16 March 2012

*Keywords:*
Nitrogen doping
Fluorine doping
P25
$TiO_2$
Photocatalysis
Photocatalytic
Cylindrospermopsin
Microcystins
Visible
UV–vis
Water treatment

ABSTRACT

In this investigation, in order to develop photocatalyst materials with improved photo-efficiency and visible light response compared to the state of the art materials, the role of Evonik Aeroxide® P25-$TiO_2$ (P25) nanoparticles incorporated in a modified sol–gel process to yield composite nitrogen and fluorine doped $TiO_2$-P25 (NF-$TiO_2$-P25) films was investigated. The addition of P25 nanoparticles in the sol leads to higher BET surface area, pore volume, porosity and total $TiO_2$ mass, as well as larger thickness and roughness of the films after heat treatment. Microscopy techniques confirmed partial sintering of NF-$TiO_2$ sol–gel formed and P25 nanoparticles having different average size. The existence of well defined regions of only anatase from NF-$TiO_2$ and anatase–rutile mix from P25 was verified in the micro-Raman spectra. The photocatalytic degradation of four microcystins (microcystin-LR, -RR, -LA and -YR) and cylindrospermopsin was evaluated with NF-$TiO_2$ and NF-$TiO_2$-P25 films under visible and UV–vis light. The general reactivity for the microcystins under acidic conditions (pH 3.0) was: MC-LA > MC-LR ≥ MC-YR > MC-RR where the highest initial degradation rate was achieved with the NF-$TiO_2$-P25 films (5 g $L^{-1}$ of P25 in sol when irradiated with visible light and 15 g $L^{-1}$ of P25 in sol when irradiated with UV–vis light). Cylindrospermopsin showed negligible adsorption at pH 3.0 for all films. Nevertheless, significant photocatalytic removal was found under UV–vis light with maximum P25 loaded films indicating that the degradation was mediated by the involvement of photogenerated reactive oxygen species and not by the trapping reaction of the positive hole.



## 1. Introduction

The presence of cyanotoxins in surface waters has been reported and documented throughout the literature [1–8]. Cyanotoxins are highly toxic secondary metabolites that can be produced by cyanobacteria during harmful bloom events. They can also be released into the water after cell lyses, which may be caused by mechanical forces in drinking water treatment plants. Cyanotoxins in water are a potential health risk to humans and aquatic life. The most commonly occurring cyanotoxins reported are microcystins (MCs) and more recently cylindrospermopsin (CYN). The general structure of microcystins and the chemical structure of CYN are depicted in Fig. 1S. Microcystins are monocyclic heptapeptide hepatotoxins with five invariant amino acids and two variant L-amino acids in the structure, which are related to the name of the molecule. For instance, microcystin-LR (MC-LR) derives from the presence of the amino acid leucine (L) and arginine (R) in these variant positions and is the most toxic and most frequently found cyanotoxin. Other commonly detected variants include MC-RR, MC-YR and MC-LA, however, more than 90 derivatives are known so far. Several species of cyanobacteria produce MCs including *Anabaena* spp., *Oscillatoria* spp., and *Microcystis aeruginosa* [4]. Microcystins' mode of action consists of the inhibition activity of the protein phosphatases types 1 and 2A (PP1 and PP2A) which categorized them as potent tumor promoters.

Advances in analytical chemistry have helped identify the cyanotoxin, CYN, a tricyclic alkaloid consisting of a tricyclic guanidine moiety bridged to a hydroxymethyluracil group that is highly soluble in water [4,6,9–12]. Several species of cyanobacteria have been identified producing CYN, such as *Cylindrospermopsis raciborskii*,

* Corresponding author. Tel.: +1 513 556 0724; fax: +1 513 556 2599.
*E-mail address:* dionysios.d.dionysiou@uc.edu (D.D. Dionysiou).

0926-3373/$ – see front matter © 2012 Elsevier B.V. All rights reserved.
doi:10.1016/j.apcatb.2012.03.010

*Aphanizomenon ovalisporum*, and *Raphidiopsis* spp. [4,6]. They are predominantly found in tropical and subtropical regions but their spatial distribution has extended to temperate zones, including the United States and other northern hemisphere countries [10]. CYN has neurotoxic effects (inhibition of protein synthesis by binding to liver DNA and forms single DNA adducts which results in liver damage), hepatotoxic effects (inhibition of glutathione synthesis in hepatocytes), and cytotoxic effects (inhibitor of cytochrome p450) [11]. Moreover, CYN has been found to be relatively stable when exposed to different environmental factors (e.g., pH, temperature) [12].

Conventional treatment processes in drinking water plants (e.g., coagulation, flocculation, sedimentation and filtration) are inadequate for the removal of cyanotoxins [13], nevertheless these cyanotoxins are susceptible to chemical oxidation. Common oxidants, such as chlorine, chlorine dioxide and permanganate, have been able to oxidize several microcystin analogues and CYN. In the case of chlorine, a dose of 1.5 mg $L^{-1}$ with a reaction time of 30 min was sufficient for at least 90% oxidation of MC-LR, MC-RR, MC-LA and MC-YR in two natural water samples [13]. The general reactivity towards chlorine was MC-YR > MC-RR > MC-LR > MC-LA and it was related to the structural differences of the functional groups present in the cyanotoxins with respect to chlorine. CYN chlorination at pH 7.0 had the maximum oxidation rate according to Rodriguez et al. [14]. The predominant species at circumneutral pH is HOCl, the most reactive form of chlorine, and can react with the dissociated form of CYN. Chlorine dioxide and permanganate are weaker oxidants and were inefficient to remove MCs and CYN due to their low reaction kinetic constants (<1 $M^{-1}$ $s^{-1}$) [15]. The removal of MC-LR, MC-RR and MC-LA, as well as CYN, via ozonation ($O_3$) was successfully achieved as well as with CYN [15–18]. The reactivity of MC-LR was slightly faster than that of MC-RR during ozonation of algae-laden source water [16]. The degradation efficiency was influenced by the effect of the dissolved organic matter present in solution which inhibits $O_3$ treatment. Spiked samples with MC-LR and MC-LA from two Australian reservoir waters (Edenhope and Myponga) were also subjected to batch ozonation [17]. It was found that a dose of 0.5 and 1.0 mg $L^{-1}$ was necessary to achieve complete removal of the toxins for Myponga and Edenhope samples, respectively. Differences between the degradation efficiencies were due to the substantially different water quality parameters. In a separate study, a static dose of 0.38 mg $L^{-1}$ of $O_3$ was used by Rodriguez et al. [15] to achieve a degradation of approximately 95% of CYN spiked in a eutrophic Swiss lake (Lake Greifensee) sample.

Recently, advanced oxidation processes (AOPs) have been established as an alternative to conventional chemical oxidation. These so-called AOPs are based on the formation of highly oxidizing and non-selective hydroxyl radical that exhibit higher second-order rate constants ($10^8$–$10^9$ $M^{-1}$ $s^{-1}$) than those of other oxidants [19]. Among AOPs, titanium dioxide ($TiO_2$) photocatalysis has gained significant attention for drinking water treatment due to its capacity to destroy recalcitrant organic contaminants [20–22]. The photocatalytic removal of several isoforms of MCs with $TiO_2$ under UV light has been investigated by many groups [23–28]. Lawton et al. [25] evaluated the influence of the solution pH on the surface interaction of MC-LR, -RR, -LW, and–LF with $TiO_2$ and the photocatalytic removal with UV light. Higher degradation rates were related to the higher extent of adsorption of the MCs at acidic pH values compared to alkaline values. Shephard et al. [26,27] used $TiO_2$ in suspension and immobilized as films illuminated with UV-C light for the removal of MC-LR, -YR and -YA. The effects of photolysis, $TiO_2$ loading, oxygen flow and the lake water matrices were investigated. Relatively high microcystin degradation rate constants ($0.25 \pm 0.01$ $min^{-1}$ for MC-LR and $0.19 \pm 0.01$ $min^{-1}$ for MC-RR) were achieved in synthetic water but slower degradation rate constants were obtained in natural water samples ($0.11 \pm 0.01$ $min^{-1}$ for MC-LR and $0.09 \pm 0.008$ $min^{-1}$ for MC-RR). Limited literature is found on the photocatalytic degradation of CYN with $TiO_2$ photocatalysis. Senogles et al. [28] used two commercially available $TiO_2$ nanoparticles under UV light to examine their efficiency on the degradation of this cyanotoxin. Several water parameters such as pH, dissolved organic carbon, temperature and initial CYN concentration were evaluated and high degradation efficiencies (75–80% at pH 4.0) were obtained indicating the feasibility of this photocatalyst for CYN degradation under UV light.

Second generation $TiO_2$ photocatalysis, where visible light photoactivation is possible via non-metal doping, has already being recognized as a potential and sustainable alternative for environmental remediation [29–32], including the treatment of drinking water supply sources contaminated with cyanotoxins [33–39]. Nitrogen and fluorine doped $TiO_2$ (NF-$TiO_2$) photocatalytic films have been successfully synthesized by a fluorosurfactant-assisted sol–gel method and the effectiveness of this catalyst was demonstrated for the photocatalytic degradation of MC-LR under visible light irradiation [35]. The incorporation of Evonik P25 nanoparticles into the sol can improve the NF-$TiO_2$ film physicochemical and optical properties. Chen and Dionysiou [40] developed a porous $TiO_2$-P25 composite film by modifying a previous method [41] by using low P25 loading (10 g $L^{-1}$) in the surfactant-assisted sol formulation employed. Following heat treatment, the film showed bimodal mesopore structure and good structural integrity [40]. The composite films demonstrated higher photocatalytic activity towards the degradation of creatinine as compared to pristine $TiO_2$ films. In addition, the composite mix of P25 nanoparticles and NF-$TiO_2$ should contribute to a more efficient utilization of the solar spectrum towards the photocatalytic degradation of cyanotoxins in water. In this study, we investigated the role of Evonik P25 in the physicochemical properties of NF-$TiO_2$-P25 composite films. The application of such composite $TiO_2$ films for the remediation of water contaminated with cylindrospermopsin and four microcystins (i.e., MC-LR, MC-RR, MC-YR and MC-LA) was further explored, under visible and UV–vis light.

## 2. Materials and methods

### 2.1. Reagents and sample preparation

MC-LR and MC-RR standards were obtained from Calbiochem. Other microcystin isoforms, such as MC-YR and MC-LA were obtained from Sigma and CYN was purchased from GreenWater Laboratories (Palatka, FL, USA). NF-$TiO_2$ was prepared using a modified sol–gel method previously developed [35]. In brief, a flurosurfacant (Zonyl FS 300, Fluka) was used as a pore template and fluorine dopant and ethylenediamine (Fisher) as nitrogen precursor. The fluorosurfactant was dissolved in isopropyl alcohol (99.8%, Pharmco), followed by the addition of acetic acid (glacial, Fisher) and ethylenediamine. Titanium tetraisopropoxide (Aldrich, 97%) was added dropwise to the sol and more acetic acid was added for peptidization. A stable sol was obtained after stirring overnight at room temperature. For the preparation of the mixed NF-$TiO_2$-P25, Aeroxide® P25-$TiO_2$ powder (Evonik; BET surface area of 53.9 $m^2$ $g^{-1}$, pore volume of 0.172 $m^3$ $g^{-1}$, 70% anatase/30% rutile) was added in each modified sol at a concentration of 5 and 15 g $L^{-1}$ and sonicated for 15 min to improve dispersion. The pristine and composite films were immobilized on borosilicate glass substrates by dip-coating with a withdrawal velocity of $12.5 \pm 0.3$ cm $min^{-1}$ and a total covered surface area of 10 $cm^2$. High temperature treatment was performed in a multi-segment programmable furnace (Paragon HT-22-D, Thermcraft) in air atmosphere where the

temperature was increased at a ramp rate of 60 °C $h^{-1}$ to 400 °C, maintained for 30 min and cooled down naturally. The dip-coating and calcination procedures were repeated until three layers were obtained.

### 2.2. Characterization of the films

A Tristar 3000 (Micromeritics) porosimeter analyzer was employed for the determination of BET surface area, pore volume, porosity, BJH pore size distribution of the NF-$TiO_2$-P25 films. The samples were scraped from the substrate, collected as powder and purged with nitrogen gas for 2 h at 150 °C using Flow prep 060 (Micromeritics). A JEM-2010F (JEOL) high resolution-transmission electron microscope (HR-TEM) with field emission gun at 200 kV was used to obtain information on crystal size and crystal structure. The samples were dispersed in methanol (HPLC grade, Pharmco) using an ultrasonicator (2510R-DH, Bransonic) for 5 min and fixed on a carbon-coated copper grid (LC200-Cu, EMS). The film morphology was characterized with an environmental scanning electron microscope (ESEM, Philips XL 30 ESEM-FEG) at an accelerating voltage of 30 kV. A Burleigh's atomic force microscopy (AFM) Metris 2000 instrument was used to observe the surface roughness of the synthesized films. Micro-Raman spectroscopy (Renishaw inVia Reflex) was applied for studying the microstructure and phase composition of the NF-$TiO_2$-P25 composite films. Raman spectra were collected in backscattering configuration, using the excitation lines of an $Ar^+$ ion laser ($\lambda$ = 514 nm) and a crystal diode laser ($\lambda$ = 785 nm). The laser beam was focused on the samples surface using a 50× objective producing spots of approximately 1.0 and 1.5 μm for the 514.5 and 785 nm laser lines, respectively. Diffuse reflectance and transmittance measurements were carried out in the range of 300–700 nm employing a Hitachi 3010 spectrophotometer equipped with a 60 mm diameter integrating sphere. By using a light trap placed opposite to the inserted beam direction, light transmitted rectilinear through the film is excluded from the integration by the sphere. In this way, the transmittance haze is calculated according to the formula $H = T_{dif}/T_{tot}$, where $T_{dif}$ is the diffuse component and $T_{tot}$ is the sum total light transmitted from the films.

### 2.3. Photocatalytic experiments

For the photocatalytic degradation of the different cyanotoxins, an aqueous solution previously adjusted to pH 3.0 ± 0.1 with $H_2SO_4$ was spiked with one or a mixture of cyanotoxins to obtain an initial molar concentration of 0.5 μM for each. A borosilicate glass vessel reactor containing the solution was sealed with parafilm and cooled down with a fan to prevent evaporation. When the experiments were performed in the visible range, the solution was irradiated with two 15 W fluorescent lamps (Cole-Parmer) mounted with UV block filter (UV420, Opticology) with a light intensity of $7.81 \times 10^{-5}$ W $cm^{-2}$ determined with a radiant power meter (Newport Corporation). The evaluation of UV–vis irradiation was performed by removing the filter from the system and the light intensity was determined to be $9.52 \times 10^{-5}$ W $cm^{-2}$. The emitted spectrum distribution of the lamps with and without the UV block filter has been previously reported [36].

All samples were analyzed with liquid chromatography (LC, Agilent Series 1100), however, the analytical method varied for certain MCs and for CYN. In the case of MC-LR and MC-YR, the analytical conditions were similar to those reported by Antoniou et al. [23] but the column employed was a $C_{18}$ Discovery (Supelco) column (150 mm × 2.1 mm, 5.0 μm particle size). The mobile phase was 60% of 0.05% trifluoroacetic acid (TFA) in water (A) and 40% of 0.05% TFA in acetonitrile (B). The flow rate was 0.2 mL/min, the injection volume was 20 μL and the wavelength for detection was set at 238 nm. For MC-RR and MC-LA, a gradient elution method was adapted from [42]. The starting condition (time = 0 min) was 25% B and increased to 75% B after 5 min, and thereafter decreased to 70% B at 6 min and back to 25% B at 6.1 min with a total sample run of 10 min. The flow rate, column temperature and injection volume were kept constant except for MC-LA where the injection volume was 50 μL and the wavelength for detection was set at 238 nm. Finally, 100% of 0.05% TFA in water was employed isocratically as mobile phase to detect CYN. Also, the flow rate, column temperature and injection volume were 0.2 mL/min, 40 °C and 20 μL, respectively. In this case, the wavelength for detection was set at 262 nm. For the sample containing a mixture of MCs, another gradient method was employed. In this case, the starting condition was 40% methanol (A) and 60% 10 mM formic acid (B). Then it was increased to 90% A and 10% B after 18 min and kept constant until 24 min. At 24.1 min, B was decreased to 40% and A increased to 60% and kept constant until the end of the run at 38 min. The column employed was a C8 Eclipse-XDB column, with a flow rate of 0.5 mL/min, temperature of 25 °C, an injection volume of 50 μL and a detection wavelength set at 238 nm. All the experiments were conducted in an Advance SterilChemgard III Class II biological safety cabinet (Baker Company, Sanford, ME) with full exhaust since MC-LR is highly toxic and irritant so appropriate handling of the toxins is needed. All the experiments were performed in triplicates and the standard error from the mean is represented by vertical error bars on the graphs. The average coefficient of variation was 15% between the experiments.

## 3. Results and discussion

### 3.1. Surface morphology of films

The overall surface morphology of the NF-$TiO_2$-P25 composite materials was examined by SEM. In the absence of P25, a rough but fairly uniform surface was observed from Fig. 1a. The presence of P25 can be clearly observed in Fig. 1b and c and the surface area covered by these nanoparticles per substrate's area increased as the P25 loading in the sol increased from 5 g $L^{-1}$ to 15 g $L^{-1}$. The aggregates comprise of clusters of P25 nanoparticles of different sizes and also some secondary particles may have formed from the alkoxide hydrolysis (see HR-TEM for additional discussion). Nevertheless, the addition of P25 did not lead to the formation of cracks, which indicates good adhesion and stability of the material retained on the support after calcination, even though the overall surface morphology changed with the presence of P25 aggregates.

The roughness of the as-synthesized films was examined with AFM. From Fig. 2a, a rough and porous surface can be observed which is characteristic of NF-$TiO_2$ film synthesized by the sol–gel method mentioned above [29]. The mean roughness obtained for NF-$TiO_2$ was 201 nm while for the film obtained from the sol containing 5 g $L^{-1}$ and 15 g $L^{-1}$ P25 was 249 and 275 nm, respectively. The grain size varies, which indicates the presence of P25 aggregates in Fig. 2b and c. However, rougher surface means larger surface area for the photocatalytic reactions to occur. Also, a larger light penetration in these rough surfaces is expected since the quantity of light absorbed is proportional to the size of the absorbing surface. This can enhance the absorption of photons by the catalyst and the production of reactive radical species leading to higher photocatalytic activity compared to smoother surfaces. Light scattering should not be discarded but no detrimental effect on the photocatalytic efficiency was observed when increasing the surface roughness of the as-prepared films. Furthermore, rough surfaces induce light scattering while mesoporous media can harvest light

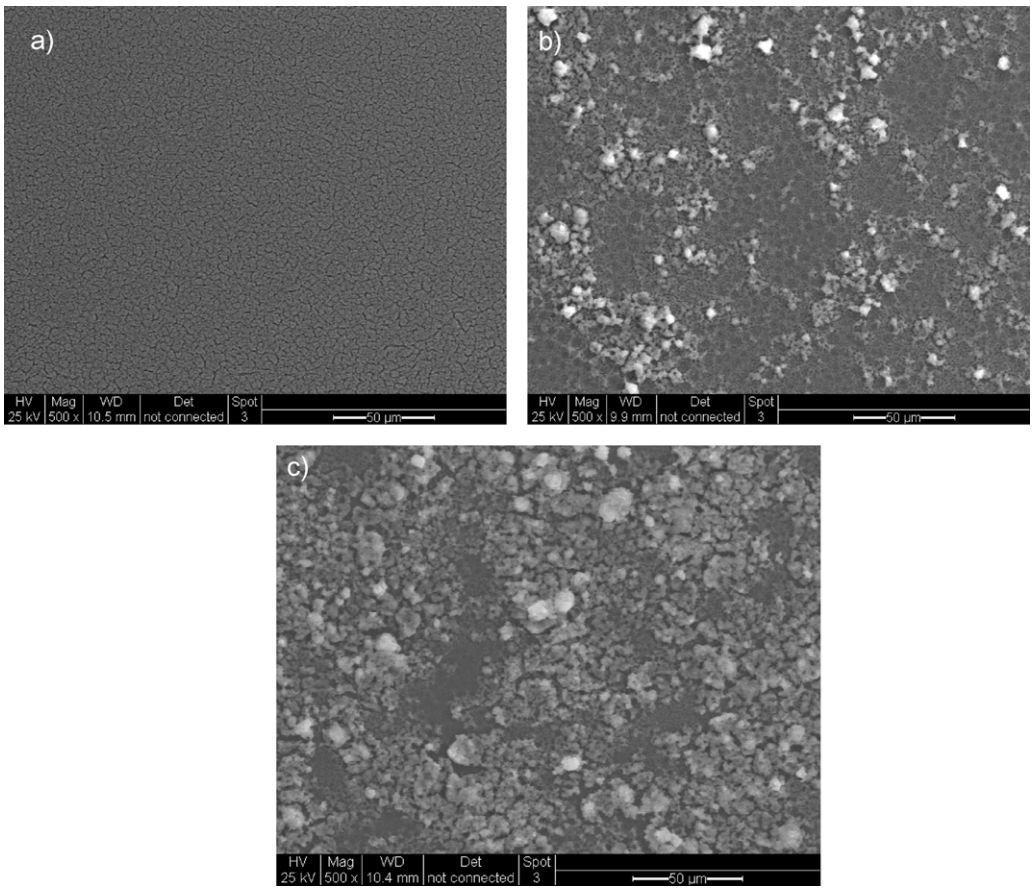


**Fig. 1.** Surface morphology of (a) NF-$TiO_2$, (b) NF-$TiO_2$-P25 (from 5 g $L^{-1}$ in sol) and (c) NF-$TiO_2$-P25 (from 15 g $L^{-1}$ in sol) films from ESEM.

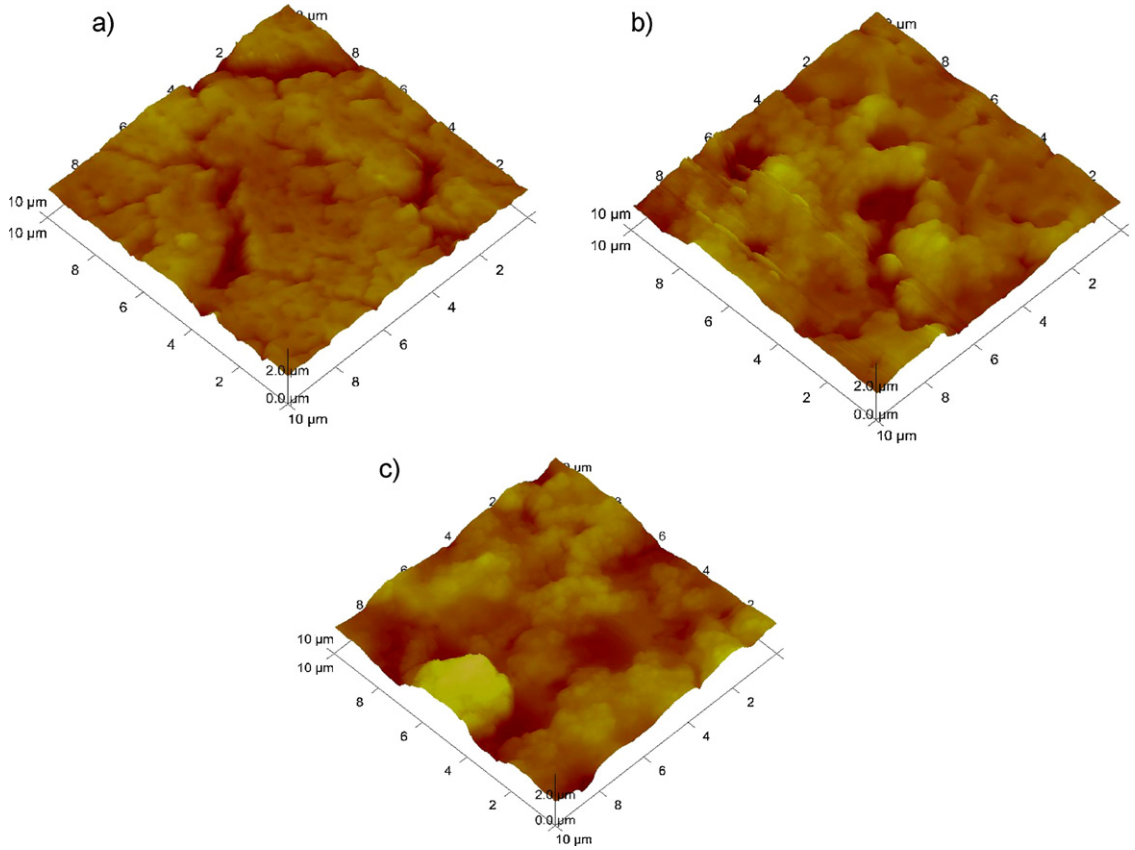


**Fig. 2.** Three-dimensional AFM image of (a) NF-$TiO_2$, (b) NF-$TiO_2$-P25 (from 5 g $L^{-1}$ in sol) and (c) NF-$TiO_2$-P25 (from 15 g $L^{-1}$ in sol) films.

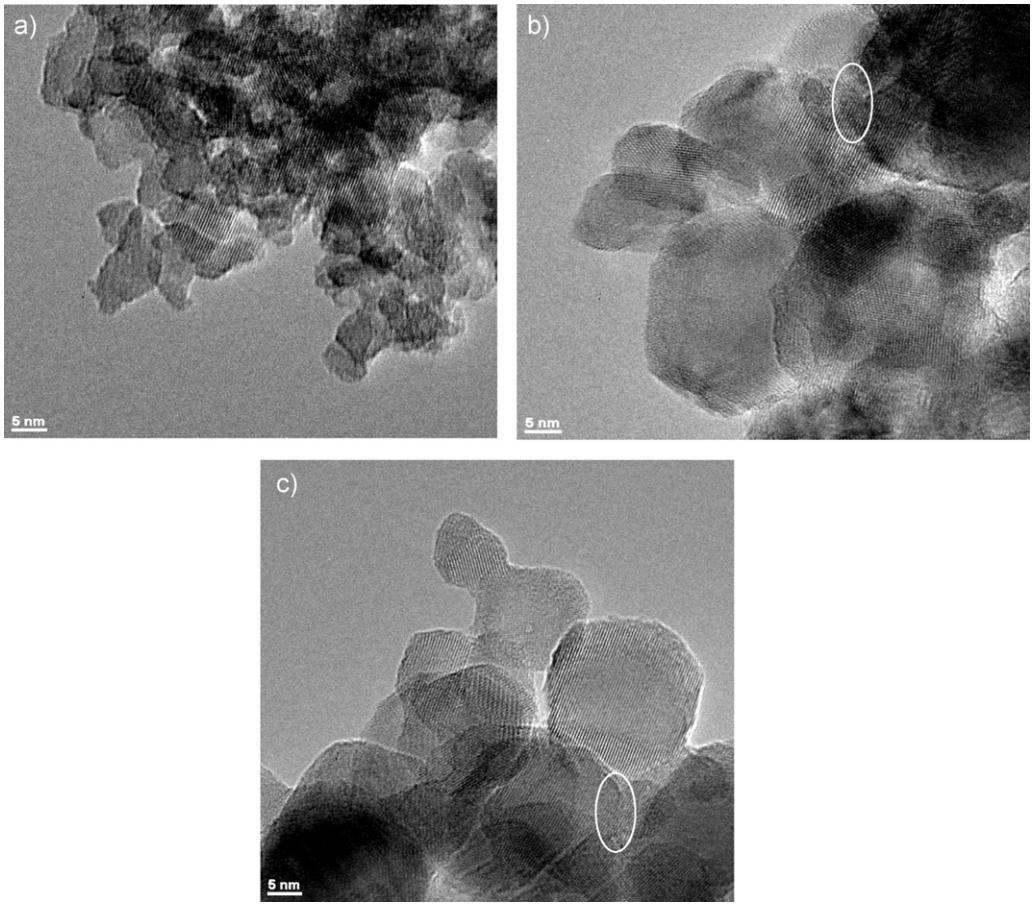


**Fig. 3.** HR-TEM image of (a) NF-$TiO_2$, (b) NF-$TiO_2$-P25 (from 5 g $L^{-1}$ in sol) and (c) NF-$TiO_2$-P25 (from 15 g $L^{-1}$ in sol).

scattered radiation via multiple reflections, thus enhancing the utilization of incident photons. Thus, the higher the surface area and roughness, the higher the light absorption (more photons) and pollutant adsorption.

Fig. 3 shows the HR-TEM images of NF-$TiO_2$ and NF-$TiO_2$-P25 composite films prepared with two different P25 loadings (5 and 15 g $L^{-1}$) in the sol. As seen in Fig. 3a, a defined, low condensed phase pore structure composed of an interconnect network with small average particle size nanoparticles was obtained from the NF-$TiO_2$ synthesis route. For Fig. 3b and c, which corresponds to 5 and 15 g $L^{-1}$ of P25 in the sol, respectively, two particle sizes can be observed and they are attributed to the presence of P25 nanoparticles and the NF-$TiO_2$ particles. The average primary particle size (obtained with ImageJ software) for both types of primary particles was 22.5 and 9.6 nm. The first value is in agreement with the typical nominal value of around 20–25 nm for P25 [43]. The second value corresponds to the particles formed from the hydrolysis and condensation of the titanium alkoxide precursor, which is in agreement to a previous study [35]. It is interesting to observe that in Fig. 3b and c, some sintering occurred between sol–gel formed nanoparticles and P25. During calcination, the NF-$TiO_2$ crystallites can be formed around the P25 nanoparticles which serve as sites of heterogeneous nucleation. A relatively larger volume ratio of alkoxide sol with respect to P25 is present and high interaction between them is expected. This can be advantageous in heterogenous processes because in such films a larger number of NF-$TiO_2$ nanoparticles can be available at the surface of the P25 particles, thus an improvement in the electron transfer at the nanoparticle interface could occur, delaying recombination of the electron–hole pair.

### 3.2. Structural, optical and crystalline composition of the films

Further information on the characterization of the films was obtained through porosimetry analysis. Table 1 summarizes the structural characteristics of NF-$TiO_2$ and NF-$TiO_2$-P25 by the modified sol–gel method. The BET surface area increased with the addition of P25 in the sol with the highest value (155 $m^2$ $g^{-1}$) at an optimum loading of 5 g $L^{-1}$. Increasing the concentration of P25 in the sol resulted in a slight increase of the pore volume and porosity.

**Table 1**
Physicochemical properties of NF-$TiO_2$ and NF-$TiO_2$-P25 from different loadings of P25 in the sol.

| Film NF-$TiO_2$-*x*P25 | BET ($m^2$ $g^{-1}$) | Pore volume ($cm^3$ $g^{-1}$) | Porosity[a] (%) | Crystal phase | Total mass of $TiO_2$ (mg) | Film thickness per layer[b] (nm) |
|---|---|---|---|---|---|---|
| *x* = 0 | 136.2 | 0.234 | 47.8 | Anatase | 6.4 | 885 |
| *x* = 5 g $L^{-1}$ | 155.1 | 0.273 | 51.5 | Anatase, rutile | 7.2 | 1059 |
| *x* = 15 g $L^{-1}$ | 149.8 | 0.314 | 55.1 | Anatase, rutile | 8.4 | 1255 |

[a] Based on pore volume and 3.9 g $cm^{-3}$ of anatase density. Porosity (%) = pore volume ($cm^3$ $g^{-1}$)/(pore volume ($cm^3$ $g^{-1}$) + solid catalyst volume without pore ($cm^3$ $g^{-1}$)) × 100; solid catalyst volume without pore ($cm^3$ $g^{-1}$) = 1/density of the solid catalyst volume without pore.

[b] Calculation based on pore volume and average film weight with average density of 3.9 g $cm^{-3}$. Film thickness = film weight per layer (g) × (pore volume ($cm^3$ $g^{-1}$) + solid catalyst volume without pore ($cm^3$ $g^{-1}$))/area of the coated support ($cm^2$).

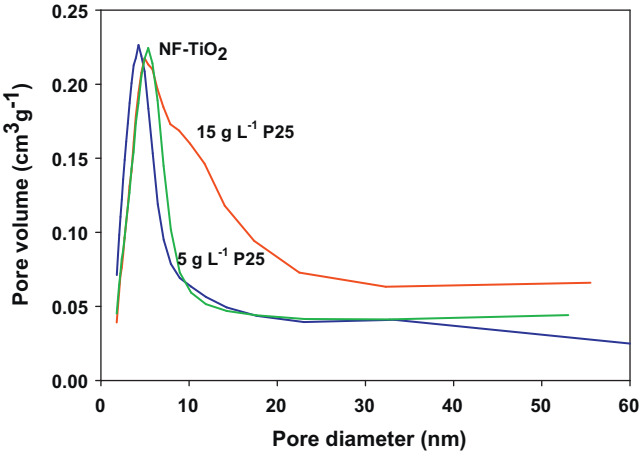


**Fig. 4.** Pore size distribution of NF-$TiO_2$ (blue line), NF-$TiO_2$-P25 (from 5 g $L^{-1}$ in sol; green line) and NF-$TiO_2$-P25 (from 15 g $L^{-1}$ in sol; red line). (For interpretation of the references to color in this figure legend, the reader is referred to the web version of the article.)

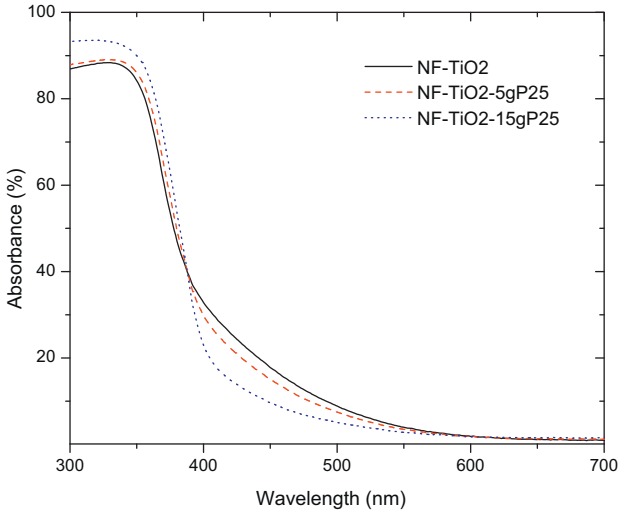


**Fig. 5.** Absorbance of the NF-$TiO_2$ and the composite NF-$TiO_2$-P25 films calculated by diffuse reflectance and transmittance spectra.

A narrow mono-modal pore size distribution with an average pore diameter of around 5 nm (see Fig. 4) was observed with NF-$TiO_2$ and with 5 g $L^{-1}$ of P25 in the sol. In the case of 15 g $L^{-1}$ P25, a broader pore size distribution is observed as is most likely due to the formation of P25-associated interparticle pores that can lead to a bimodal pore size structure. Chen and Dionysiou [40] found a bimodal pore size distribution for $TiO_2$ films synthesized from a surfactant assisted sol–gel method that contained P25 nanoparticles. The formation of this bimodal pore structure is based on the ability of the larger P25 particle to act as a kind of pore wall or building block where smaller particles from the alkoxide sol can be formed and generate a larger pore, besides the one formed from the pore template surfactant, after calcination [40]. The absence of P25 did not lead to any formation of bimodal pore size distribution, even when the concentration of the surfactant was increased, pointing out the role of P25 incorporation on inducing the formation of secondary large mesopores. This phenomenon was reflected in such significant increase in pore volume and porosity found in our study. Several other physicochemical properties were enhanced for the NF-$TiO_2$-P25 films. The total mass of $TiO_2$ immobilized on the glass substrate increased with the amount of P25 loaded in the sol (see Table 1). This provides more surface area of the catalyst in the coated area of the support that could lead to higher photocatalytic activity. The film thickness was also affected by the concentration of P25 in the sol. When 15 g $L^{-1}$ of P25 was added into the sol, a thickness of 988 nm was observed for the composite NF-$TiO_2$-P25 film as compared to 672 nm for the NF-$TiO_2$ film only. It can be clearly seen that with the addition of P25 into the sol, fewer dip coating cycles would be needed to obtain optimum film thickness with high photocatalytic activity and good mechanical stability, which is a useful approach for the synthesis of thick solar light activated $TiO_2$ films.

Recorded diffuse reflectance ($R$) and transmittance ($T$) spectra were used in order to calculate the absorbance ($A$) of the films as: $A\ (\%) = 100 - R\ (\%) - T\ (\%)$. The corresponding absorbance spectra of the NF-$TiO_2$ and the composite NF-$TiO_2$-P25 films are shown in Fig. 5. The NF-$TiO_2$ films present a significant visible light absorption component with an absorption edge estimated at 510 nm, in accordance to [44]. The increase of Evonik P25 content results in a reduction of the average visible light absorption in the 400–510 nm range, from 17.8% (NF-$TiO_2$) to 15.3% (NF-$TiO_2$ – 5 g $L^{-1}$ P25) and 10.3% (NF-$TiO_2$ – 15 g $L^{-1}$ P25). The low percentage of visible light absorption of the NF-$TiO_2$ – 15 g $L^{-1}$ P25 films explains the relatively low photocatalytic activity that these films present under visible light illumination (see Section 3.3.2). Furthermore, the haze of the samples was estimated to 80% for the NF-$TiO_2$ film and increased to above 97% for the composite films. This significant increase of haze can improve light harvesting efficiency for photo-induced processes via multiple light scattering effects, in equivalence to the role of scattering layers in dye-sensitized solar cells. In [45], $TiO_2$ nanostructured films with two layers consisting of $TiO_2$ particles having average diameters of 9 and 20 nm were fabricated, presenting also a very high haze of about 97%. Although the $TiO_2$ photoelectrodes have two distinct layers, in opposite to our case where one layer with mixed particles was obtained, the two particle sizes are similar to the ones obtained in this work (~9 nm for NF-$TiO_2$ and 21 nm for Evonik P25).

Raman measurements of the NF-$TiO_2$ and P25 reference films were firstly recorded. Results obtained by excitation under visible (Fig. 6) and near infrared (NIR) (Fig. 2S) show very similar characteristics. The signal from the NF-$TiO_2$ samples presents a huge fluorescence background at both excitations, probably due to organic residues and a relatively low signal of the Raman peaks, where only the intense anatase peak $E_g$ peak at 144 $cm^{-1}$ is clearly

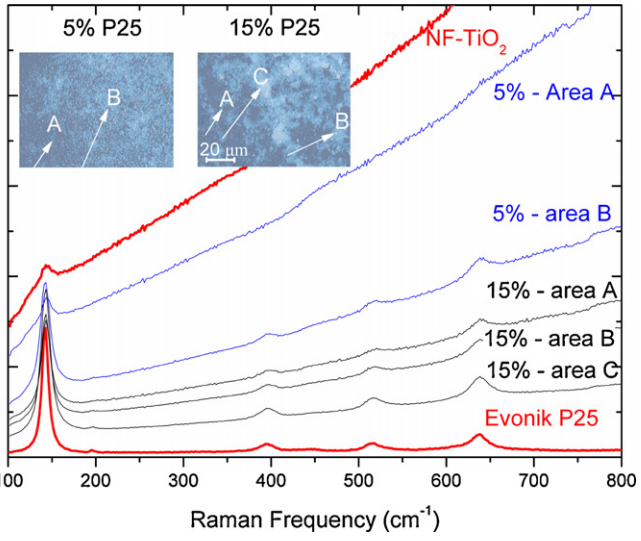


**Fig. 6.** Raman spectra excited under 514 nm of the reference NF-$TiO_2$ and Evonik P25 films as well as of composite films with 5 and 15 g $L^{-1}$ Evonik P25 content from different samples' areas. Optical microscope photographs of the two composite films with marked areas of Raman signal detection are shown as an inset.

observed. On the other hand, the Raman spectra of P25 particles are background free and present a set of well resolved bands (143, 194, 393, 514 and 637 $cm^{-1}$) due to the predominant anatase phase as well as a weak peak at 446 $cm^{-1}$ of the minor rutile phase. The Raman signal of the composite films is a combination of the two material independent signals verifying the efficient crystalline formation. The Raman spectra differ significantly from point to point suggesting distinct phase segregation in the micrometer scale that matches the regions defined in the optical microscope images. Spectra were recorded from different surface regions of the films that look differently under the optical microscope, as shown in the inset photographs of Fig. 6. Thus, dark areas (A) are rich of NF-$TiO_2$, white areas present mixed NF-$TiO_2$ and Evonik P25 phases while bright white areas (C) are mainly composed from P25 nanoparticles. In fact, the films with 5 g $L^{-1}$ P25 have majority of NF-$TiO_2$ nanoparticles with dominant dark regions (A) and a few white regions (B). For the films with the maximum P25 content (15 g $L^{-1}$), white regions (B) exceed the dark ones (A) and occasionally bright white regions (C) are seen, in consistence with the large content of P25 nanoparticles.

### 3.3. Photocatalytic evaluation of the composite films

#### 3.3.1. Adsorption of MCs and CYN in the dark

Control experiments under dark conditions (absence of light) were performed to evaluate the extent of adsorption of each MC and CYN with NF-$TiO_2$ and NF-$TiO_2$-P25 composite films. Table 2 shows the percentage adsorption of each MC and CYN after 5 h at pH 3.0. The film prepared from the sol with 15 g $L^{-1}$ of P25 showed the highest percentage adsorption for all MCs due to the enhanced structural and physicochemical properties (see Table 1). The formation of a bimodal pore size structure can increase the interaction between the mesoporous structure and the MCs, facilitate the transport to the active sites and improve photocatalytic activity. For all the films synthesized, the adsorption of MC-YR was the highest followed by MC-LA, then MC-LR and finally MC-RR. Under pH 3.0, the net charge of MC-YR, MC-LA and MC-LR is negative (due to the ionization of the carboxylic groups present in most MCs' cyclic structure) and the photocatalyst is positively charged (point of zero charge of NF-$TiO_2$ and P25 is around 6.3 [34]), while MC-RR is also positive at pH 3.0 [25]. The two amino acids in the variable positions of the microcystin molecule play a key role in determining the overall charge as well as the hydrophobic character of the molecule. Alanine and tyrosine will have a net charge of zero between pH 2.0 and 9.0 [46]. Leucine and alanine are classified as hydrophobic and tyrosine as partially hydrophobic. Arginine has a guanidinium group that is positively charged in acidic, neutral and even basic pH and is a more polar amino acid imparting hydrophilicity. Therefore, for instance, MC-RR carries a net positive charge while MC-LR carries a single negative charge at pH 3.0. The porosity and pore size of the different films can also have an impact in the adsorption of the toxins. The average molecular size of MCs is approximately 3 nm in diameter [1] compared to the average pore diameter of the films (see Fig. 4). Thus, the length of the MCs justifies the pore size requirements of the films for adsorption to occur. A broader pore size distribution from the composite film obtained with 5 and 15 g $L^{-1}$ of P25 signifies the potential of higher adsorption which was observed in the dark adsorption of MCs (see Table 2). For CYN, no significant adsorption was observed with the three different films since the toxin is overall positively charged (like the NF-$TiO_2$ films) and very hydrophobic at pH 3.0. All these indicate that dark adsorption of the tested cyanotoxins onto NF-$TiO_2$ is pH dependent and the electrostatic interaction and the hydrophobicity, as well as the structural properties of the composite films, can have a significant effect in the overall adsorption of these toxins on NF-$TiO_2$.

**Table 2**
Extent of adsorption of MC-LR, MC-RR, MC-YR, MC-LA and CYN under dark conditions after 5 h with NF-$TiO_2$ and NF-$TiO_2$-P25. Initial molar concentration of each cyanotoxin: 0.5 μM.

| Film | Dark adsorption after 5 h (%) | | | | |
|---|---|---|---|---|---|
| | MC-LR | MC-RR | MC-LA | MC-YR | CYN |
| NF-$TiO_2$ | 16.3 | 8.8 | 26.5 | 40.9 | <1 |
| 5 g $L^{-1}$ P25 | 26.4 | 9.8 | 37.1 | 43.9 | <1 |
| 15 g $L^{-1}$ P25 | 32.3 | 10.5 | 45.2 | 44.2 | <1 |

#### 3.3.2. Photocatalytic activity under visible light

NF-$TiO_2$ and NF-$TiO_2$-P25 films were firstly investigated for the photocatalytic degradation of the different MCs and CYN in aqueous solutions under visible light illumination at pH 3.0. Fig. 7a shows the MCs initial degradation rates obtained with the different synthesized films by considering the first 180 min of reaction time. It is important to notice that despite the incorporation of different P25 loadings in the modified sol (5 and 15 g $L^{-1}$), the synthesized composite films remained photocatalytically active under visible light. In fact, the initial degradation rate increased for almost all MCs tested for both composite

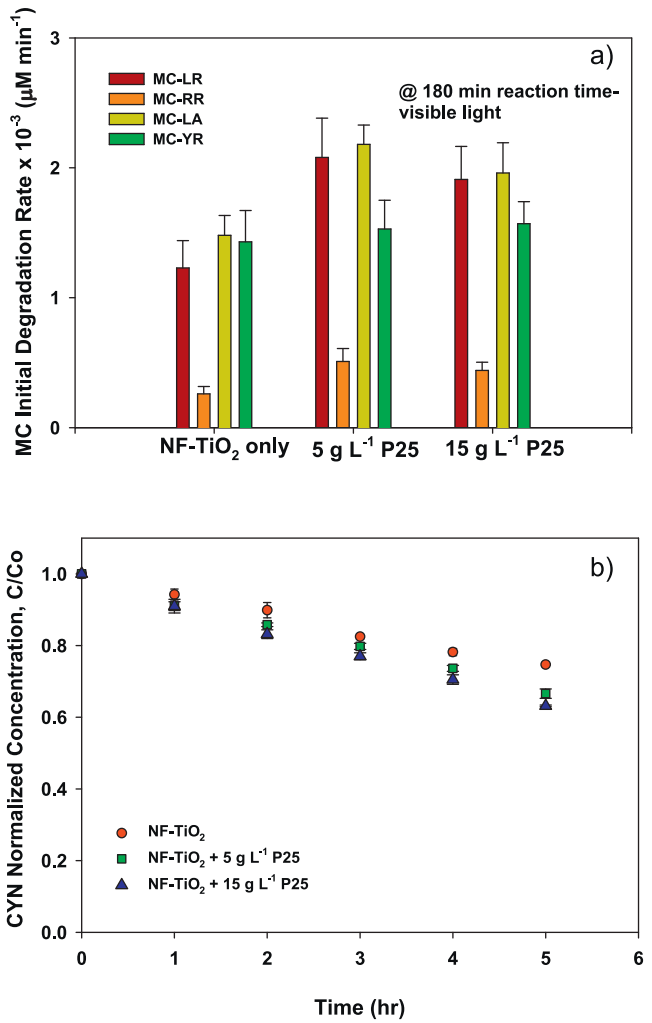


**Fig. 7.** (a) Initial degradation rates of MC-LR, MC-RR, MC-LA and MC-YR (initial molar concentration for each cyanotoxin: 0.5 μM) with NF-$TiO_2$ and NF-$TiO_2$-P25 under visible light (λ > 420 nm) at pH 3.0 after 180 min of reaction and (b) photocatalytic degradation of cylindrospermopsin under visible light (λ > 420 nm) with NF-$TiO_2$ and NF-$TiO_2$-P25 at pH 3.0.

NF-$TiO_2$-P25 films, with the highest achieved when adding 5 g $L^{-1}$ P25 in the sol. For instance, the initial degradation rate of MC-LA increased from $1.48 \pm 0.15 \times 10^{-3}$ μM $min^{-1}$ with NF-$TiO_2$ to $2.18 \pm 0.14 \times 10^{-3}$ μM $min^{-1}$ with NF-$TiO_2$-P25 (from 5 g $L^{-1}$ in sol) and it can be attributed to the enhanced physicochemical properties of the composite films. Even though the highest microcystin adsorption equilibrium was obtained with 15 g $L^{-1}$ of P25 in the sol, the highest initial degradation rate was with 5 g $L^{-1}$, indicating that an excess of P25 in the film can decrease the reactivity under visible light, despite the improvement in some properties such as pore volume, porosity and total mass of $TiO_2$ in the support. The general reactivity of all tested films towards the MCs was the following: MC-LA > MC-LR ≥ MC-YR > MC-RR with the highest initial degradation rate achieved with NF-$TiO_2$-P25 (5 g $L^{-1}$ in sol) under acidic conditions. The difference in reactivity can be rationalized in terms of molecular weight and structure configuration, where a steric effect of the variable amino acids can hinder the reactive oxygen species (ROS) generated from attacking other more susceptible functional groups in the molecule. Even though the visible light activated mechanism of ROS formation with non-metal doped $TiO_2$ may not directly involve hydroxyl radicals [29], the Adda moiety is generally considered as the preferential site of attack [23,47]. Antoniou et al. [23] reported that the conjugated double bonds of the Adda moiety are the preferred site of hydroxyl radical attack for MC-LR. Singlet oxygen oxygenation and electronic energy transfer have also been responsible of the transformation of the Adda moiety [47]. MC-RR contains an additional larger arginine group, compared to MC-LR, which can block the ROS from reacting with the Adda chain leading to decrease of reactivity. Therefore, the degradation process for the MCs is a function of the surface interaction between each MC and the photocatalyst which is affected by the pH of the solution (see Section 3.3.1) and the structural differences due to the functional groups present in each microcystin that can undergo ROS attack for degradation.

Fig. 7b shows the degradation profile of CYN with NF-$TiO_2$ and NF-$TiO_2$-P25 under visible light. Since the adsorption of CYN was negligible at pH 3.0 with all films tested, low degradation rates were observed for this toxin under visible light. Nevertheless, a similar trend to that found with MCs was observed where the composite NF-$TiO_2$-P25 showed higher removal of CYN compared to NF-$TiO_2$ only. This also confirms that indeed the films can still be activated under visible light and photogenerate ROS to degrade the toxins, even though there is insignificant surface interaction between the photocatalyst and CYN at pH 3.0. Senogles et al. [28] suggested that the degradation of cylindrospermopsin at low pH values involves diffusion of the photocatalytically generated radicals away from the surface of the semiconductor into the bulk solution. Turchi and Ollis proposed that organic compounds could react in the proximity of the $TiO_2$ surface with the photo-generated ROS and not by the trapping reaction of the positive hole [48].

### 3.3.3. Photocatalytic activity under UV–vis light

The MCs initial degradation rates (after 180 min reaction time) with NF-$TiO_2$ and with the two NF-$TiO_2$-P25 composite films under UV–vis light are shown in Fig. 8a. As expected, the initial degradation rates are higher compared to the rates obtained under visible light. For example, MC-RR had the lowest initial degradation rate with NF-$TiO_2$-P25 ($0.51 \pm 0.09 \times 10^{-4}$ μM $min^{-1}$ and $0.44 \pm 0.06 \times 10^{-4}$ μM $min^{-1}$ for 5 and 15 g $L^{-1}$ P25 in the sol, respectively) under visible light but it increased to $1.84 \pm 0.12 \times 10^{-3}$ μM $min^{-1}$ and $1.88 \pm 0.13 \times 10^{-3}$ μM $min^{-1}$, almost an order of magnitude higher, under UV–vis light. The rest of the MCs also exhibited higher initial degradation rates under UV–vis light in the presence of the tested photocatalyst. The photocatalytic degradation kinetics of CYN with NF-$TiO_2$ and NF-$TiO_2$-P25 under UV–vis light are depicted in Fig. 8b. The performance of all synthesized films was significantly better under UV–vis light compared to visible light irradiation; therefore high photocatalytic removal of CYN was obtained after 5 h of reaction time. Increasing the concentration (from 5 to 15 g $L^{-1}$) of P25 in the sol enhanced the photocatalytic activity, leading to a complete removal of CYN after 4 h. For the solar-driven photocatalytic degradation of MCs and CYN, the use of UV–vis light included UV radiation with peaks at around 310, 356 and 410 nm that can be observed in the absence of the filter employed, according to the light spectrum previously reported [36]. Therefore, the light intensity was higher for UV–vis ($9.52 \times 10^{-5}$ W $cm^{-2}$) than that for visible light ($7.81 \times 10^{-5}$ W $cm^{-2}$). P25 nanoparticles have been proven to be highly active under UV light [40,43] as well as NF-$TiO_2$ film (compared to reference $TiO_2$ in [35]), therefore the contribution of the UV photoactivation of NF-$TiO_2$ and P25 enhanced the photocatalytic degradation of cyanotoxins under UV–vis light. In this case, increasing P25 loading in the film along with the higher surface area, film thickness and porosity obtained during synthesis resulted in higher photocatalytic activity.

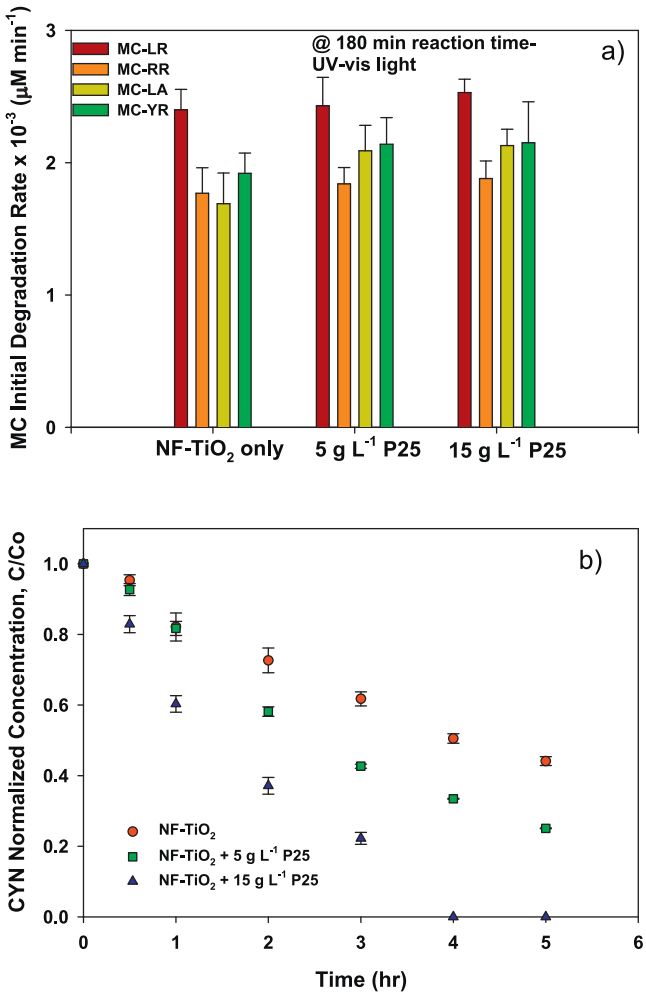


**Fig. 8.** (a) Initial degradation rates of MC-LR, MC-RR, MC-LA and MC-YR (initial molar concentration for each cyanotoxin: 0.5 μM) with NF-$TiO_2$ and NF-$TiO_2$-P25 under UV–vis light at pH 3.0 after 180 min of reaction and (b) photocatalytic degradation of cylindrospermopsin under UV–vis light with NF-$TiO_2$ and NF-$TiO_2$-P25 at pH 3.0.

The presence of MCs in surface water is typically found as a mixture since their production and release from cyanobacteria can occur simultaneously during blooms or after cell lyses. For this reason, a solution containing a mixture of MC-LR, -RR,

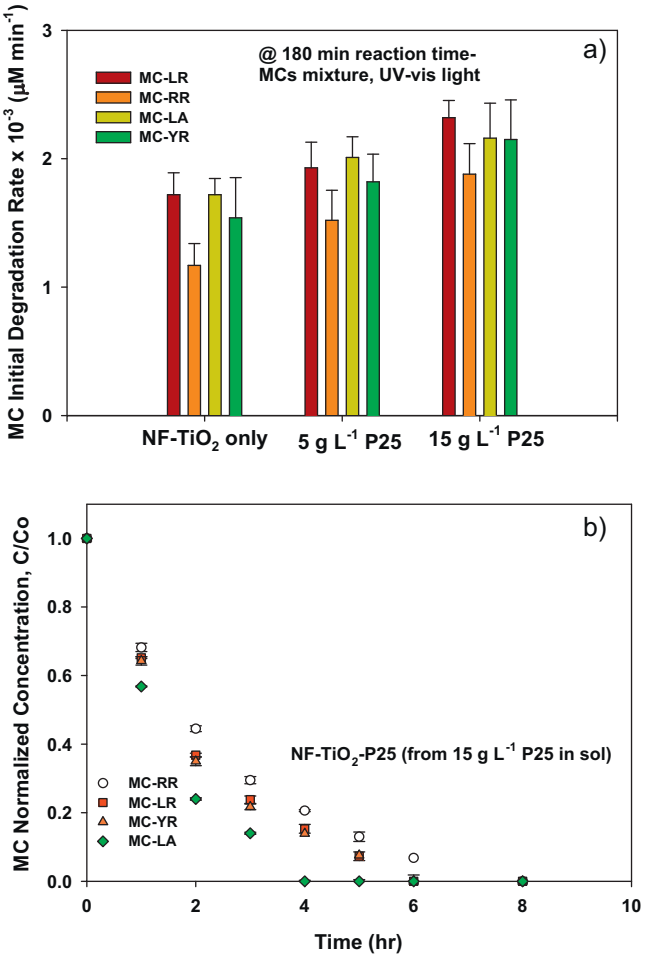


**Fig. 9.** (a) Initial degradation rates of MC-LR, MC-RR, MC-LA and MC-YR from a mixed solution at pH 3.0 (initial molar concentration for each cyanotoxin: 0.5 μM) with NF-$TiO_2$ and NF-$TiO_2$-P25 under UV–vis light after 180 min of reaction and (b) photocatalytic degradation of a mixture of MCs with NF-$TiO_2$-P25 (from 15 g $L^{-1}$ in sol) under UV–vis light.

-YR and -RR at pH 3.0 was irradiated under UV–vis light in the presence of NF-$TiO_2$ and NF-$TiO_2$-P25 and the initial degradation rates are shown in Fig. 9a. Overall, high removal was obtained for the mixture of MCs, yet, the initial degradation rates were lower under UV–vis light compared to each individual MC (see Fig. 8a). A slightly different trend was observed compared with visible light for the photocatalytic degradation of the mixture cyanotoxins under simulated solar light with the composite films: MC-LR > MC-LA ≥ MC-YR > MC-RR. This can be attributed to the competition between the different MCs present in solution and the active sites and the ROS generated under solar light; leading also to longer reaction times compared to each individual toxin. Despite this, complete removal of all MCs was observed when employing NF-$TiO_2$-P25 (from 15 g $L^{-1}$ of P25 in sol) after 8 h of reaction time (see Fig. 9b) indicating high efficiency of this composite $TiO_2$-based film under UV–vis light.

## 4. Conclusions

Composite NF-$TiO_2$-P25 films were synthesized via wet chemistry with a modified sol–gel method. The incorporation of P25 nanoparticles in the sol played a significant role by improving the physicochemical properties of the film. An enhancement in the BET surface area, pore volume, porosity and total $TiO_2$ mass in the coated support was obtained with the addition of P25 in the sol. Two different particle sizes were identified that correspond to the NF-$TiO_2$ sol–gel formed nanoparticles and P25 with some sintering effect between them. The thickness and roughness of the film was also increased and the formation of bimodal pore size distribution at high P25 loading (15 g $L^{-1}$ in the sol) was observed. Two independent signals of crystalline anatase phase of NF-$TiO_2$ and anatase and rutile phase of P25 nanoparticles were observed in defined regions of the films according to Raman measurements. The photocatalytic activity was enhanced under visible and UV–vis light for the degradation of microcystin-LR, -RR, -LA, -YR and CYN in acidified water (pH 3.0). Higher extent of adsorption under dark conditions led to higher removal with a general reactivity towards an individual toxin or a mixture of them as follow: MC-LA ≥ MC-LR ≥ MC-YR > MC-RR. The photocatalytic degradation of cylindrospermopsin with NF-$TiO_2$-P25 films under UV–vis light showed high efficiency despite negligible adsorption at the conditions tested. This study is opening new ways for the design and development of new, innovative and very efficient titania photocatalysts and can provide insightful input for the suitable design of solar-driven nanotechnology based photo-reactors for purification of water contaminated with cyanobacterial toxins and other contaminants of emerging concern, using solar light as a renewable source of energy.

## Disclaimer

The research described in this article has not been subjected to the Agency's required peer and policy review and therefore does not necessarily reflect the views of the Agency and no official endorsement should be inferred.

## Acknowledgments

This work was funded by a NSF Collaborative Research (US-Ireland) (number CBET-1033317), co-funded by the Department of Employment and Learning, Northern Ireland; and the European Commission (Clean Water – Grant Agreement number 227017). Clean Water is a Collaborative Project co-funded by the Research DG of the European Commission within the joint RTD activities of the Environment and NMP Thematic Priorities/FP7. Helpful discussions with Dr. Vlassis Likodimos are also acknowledged.

## Appendix A. Supplementary data

Supplementary data associated with this article can be found, in the online version, at doi:10.1016/j.apcatb.2012.03.010.

## References

[1] M.G. Antoniou, A.A. de la Cruz, D.D. Dionysiou, J. Environ. Eng. 131 (2005) 1239–1243.
[2] J.L. Graham, K.A. Loftin, M.T. Meyer, A.C. Ziegler, Environ. Sci. Technol. 44 (2010) 7361–7368.
[3] A.A. de la Cruz, M.G. Antoniou, A. Hiskia, M. Pelaez, W. Song, K.E. O'Shea, X. He, D.D. Dionysiou, Anti-Cancer Agents Med. Chem. 11 (2011) 19–37.
[4] M. Pelaez, M.G. Antoniou, X. He, D.D. Dionysiou, A.A. de la Cruz, K. Tsimeli, T. Triantis, A. Hiskia, T. Kaloudis, C. Williams, M. Aubel, A. Chapman, A. Foss, U. Khan, K.E. O'Shea, J. Westrick, Xenobiotics in the Urban Water Cycle, Springer, USA, 2010.
[5] J.F. Briand, S. Jacquet, C. Bernard, J.F. Humbert, Vet. Res. 34 (2003) 361–377.
[6] J.A. Westrick, D.C. Szlag, B.J. Southwell, J. Sinclair, Anal. Bioanal. Chem. 397 (2010) 1705–1714.
[7] C. Edwards, L.A. Lawton, Adv. Appl. Microbiol. 67 (2009) 109–129.
[8] P.J. Garcia Nieto, F. Sánchez Lasheras, F.J. de Cos Juez, J.R. Alonso Fernández, J. Hazard. Mater. 195 (2011) 414–421.
[9] Cires, L. Wörmer, J. Timon, C. Wiedner, A. Quesada, Harmful Algae 10 (2011) 668–675.
[10] M. Gugger, R. Molica, B. Le Berre, P. Dufour, C. Bernard, J.-F. Humbert, Appl. Environ. Microbiol. 71 (2) (2005) 1097–1100.
[11] D.J. Griffiths, M.L. Saker, Environ. Toxicol. 18 (2) (2003) 78–93.

[12] R.K. Chiswell, G.R. Shaw, G. Eaglesham, M.J. Smith, R.L. Norris, A.A. Seawright, M.R. Moore, Environ. Toxicol. 14 (1) (1999) 155–161.
[13] L. Ho, G. Onstad, U. von Gunten, S. Rinck-Pfeiffer, K. Craig, G. Newcombe, Water Res. 40 (2006) 1200–1209.
[14] E. Rodriguez, A. Sordo, J.S. Metcalf, J.L. Acero, Water Res. 41 (2007) 2048–2056.
[15] E. Rodriguez, G.D. Onstad, T.P.J. Kull, J.S. Metcalf, J.L. Acero, U. von Gunten, Water Res. 41 (2007) 3381–3393.
[16] H. Miao, W. Tao, Sep. Purif. Technol. 66 (2009) 187–193.
[17] Brooke, G. Newcombe, B. Nicholson, G. Klass, Toxicon 48 (2006) 1054–1059.
[18] G. Onstad, S. Strauch, J. Meriluoto, G.A. Codd, U. Von Gunten, Environ. Sci. Technol. 41 (2007) 4397–4404.
[19] M. Mohajerani, M. Mehrvar, F. Ein-Mozaffari, Int. J. Eng. 3 (2) (2009) 120–146.
[20] H. Choi, E. Stathatos, D.D. Dionysiou, Desalination 202 (2007) 199–206.
[21] F. Han, V.S.R. Kambala, M. Srinivasan, D. Rajarathnam, R. Naidu, Appl. Catal. A 359 (2009) 25–40.
[22] M.N. Chong, B. Jin, C.W.K. Chow, C. Saint, Water Res. 44 (2010) 2997–3027.
[23] M.G. Antoniou, J.A. Shoemaker, A.A. de la Cruz, D.D. Dionysiou, Toxicon 51 (2008) 1103–1118.
[24] M.G. Antoniou, P.A. Nicolaou, J.A. Shoemaker, A.A. de la Cruz, D.D. Dionysiou, Appl. Catal. B 91 (1–2) (2009) 165–173.
[25] A. Lawton, P.K.J. Robertson, B.J.P.A. Cornish, I.L. Marr, M. Jaspars, J. Catal. 213 (2003) 109–113.
[26] G.S. Shephard, S. Stockenström, D. De Villiers, W.J. Engelbrecht, E.W. Sydenham, G.F.S. Wessels, Toxicon 36 (12) (1998) 1895–1901.
[27] G.S. Shephard, S. Stockenström, D. De Villiers, W.J. Engelbrecht, G.F.S. Wessels, Water Res. 36 (2002) 140–146.
[28] P.-J. Senogles, J.A. Scott, G. Shaw, H. Stratton, Water Res. 35 (5) (2001) 1245–1255.
[29] J.A. Rengifo-Herrera, K. Pierzchala, A. Sienkiewicz, L. Forro, J. Kiwi, C. Pulgarin, Appl. Catal. B 88 (2009) 398–406.
[30] J.A. Rengifo-Herrera, E. Mielczarski, J. Mielczarski, N.C. Castillo, J. Kiwi, C. Pulgarin, Appl. Catal. B 84 (2008) 448–456.
[31] J. Senthilnatan, L. Philip, Chem. Eng. J. 161 (2010) 83–92.
[32] D.P. Subagio, M. Srinivasan, M. Lim, T.-T. Lim, Appl. Catal. B 95 (2010) 414–422.
[33] H. Choi, M.G. Antoniou, M. Pelaez, A.A. De la Cruz, J.A. Shoemaker, D.D. Dionysiou, Environ. Sci. Technol. 41 (2007) 7530–7535.
[34] M. Pelaez, A.A. de la Cruz, E. Stathatos, P. Falaras, D.D. Dionysiou, Catal. Today 144 (2009) 19–25.
[35] M. Pelaez, P. Falaras, V. Likodimos, A.G. Kontos, A.A. de la Cruz, K. O'Shea, D.D. Dionysiou, Appl. Catal. B 99 (2010) 378–387.
[36] M. Pelaez, A.A. de la Cruz, K. O'shea, P. Falaras, D.D. Dionysiou, Water Res. 45 (2011) 3787–3796.
[37] C. Han, M. Pelaez, V. Likodimos, A.G. Kontos, P. Falaras, K. O'Shea, D.D. Dionysiou, Appl. Catal. B 107 (2011) 77–87.
[38] D. Graham, H. Kisch, L.A. Lawton, P.K.J. Robertson, Chemosphere 78 (2010) 1182–1185.
[39] J. Yang, D.-X. Chen, A.-P. Deng, Y.-P. Huang, C.-C. Chen, Res. Chem. Intermed. 37 (1) (2011) 47–60.
[40] Y. Chen, D.D. Dionysiou, Appl. Catal. B 80 (2008) 47–155.
[41] G. Balasubramanian, D.D. Dionysiou, M.T. Suidan, I. Baudin, J.-M. Laîné, Appl. Catal. B 47 (2004) 73–84.
[42] E.M. Rodríguez, J.L. Acero, L. Spoof, J. Meriluoto, Water Res. 42 (6–7) (2008) 1744–1752.
[43] A. Ritter, F.A. Reifler, S. Saini, Appl. Catal. A 352 (1–2) (2009) 271–276.
[44] A.G. Kontos, M. Pelaez, V. Likodimos, N. Vaenas, D.D. Dionysiou, P. Falaras, Photochem. Photobiol. Sci. 10 (2011) 350–354.
[45] J.-K. Lee, B.-H. Jeong, S.-I. Jang, Y.-S. Yeo, S.-H. Park, J.-U. Kim, Y.-G. Kim, Y.-W. Jang, M.-R. Kim, J. Mater. Sci. Mater. Electron. 20 (2009) S446–S450.
[46] G. Newcombe, D. Cook, S. Brooke, L. Ho, N. Slyman, Environ. Technol. 24 (3) (2003) 299–308.
[47] M. Welker, C. Steinberg, Environ. Sci. Technol. 34 (2000) 3415–3419.
[48] C.S. Turchi, D.F. Ollis, J. Catal. 122 (1990) 178–192.